Nanoscale

PAPER

View Article Online
View Journal

Cite this: DOI: 10.1039/d6nr00405a

Optimizing the supercapacitive performance of MoS_2 by multivalent tungsten ion doping

Ion Nesterovschi,[a,b] Ameen Uddin Ammar,[a] Adriana Popa,[a] Maria Stefan,[a] Dana Toloman,[a] Sergiu Gabriel Macavei,[a] Cristina Leostean,[a] Lucian Barbu Tudoran,[a] Maria Mihet,[a] Ana Varadi,[a,c] Emre Erdem[a,d] and Arpad Mihai Rostas *[a]

Received 29th January 2026,
Accepted 19th May 2026

DOI: 10.1039/d6nr00405a

rsc.li/nanoscale

This study examined the effect of tungsten doping on the structural and electrochemical performance of molybdenum disulfide (MoS_2) in symmetric supercapacitor devices. MoS_2 nanoflowers with different W contents (0–1%) were synthesized by a hydrothermal method and characterized using XRD, Raman, PL, EPR, SEM, and BET analysis. Tungsten incorporation induced lattice distortions, sulfur vacancies, and enhanced defect-assisted charge transport, while retaining the layered morphology. Electrochemical measurements revealed a combination of electric double-layer and pseudocapacitive behavior with the MoS_2:W0.7 electrode material delivering the highest performance. This device achieved a specific capacitance of 848 F g^{-1} at 10 mV s^{-1}, an energy density of 117.8 Wh kg^{-1}, a power density of 2121 W kg^{-1}, and excellent cycling stability, retaining 97% of its capacitance. The results demonstrate that W doping introduces additional electroactive sites and improves conductivity, highlighting a simple strategy to enhance the energy-storage capability of MoS_2-based materials for supercapacitor applications.

1 Introduction

The increasing global demand for energy and the imperative to mitigate climate change have underscored the importance of energy storage technologies. Supercapacitors (SC), characterized by high power density, rapid charge–discharge capabilities, and extended cycle life, represent a promising solution.[1] These devices can be connected to portable and wearable electronics, electric vehicles, and industrial energy management systems.[2] Unlike batteries, SCs offer unique advantages, including fast charging, long cycle life, and high power density. However, their energy density is lower than that of batteries, necessitating further research to improve their performance.[3]

Supercapacitors store energy through two primary mechanisms: ion adsorption at the electrode surface (electric double-layer capacitor, EDLC) and fast, reversible faradaic redox reactions at or near the electrode surface (pseudocapacitors).[4] EDLCs, made from materials like activated carbon, graphene, and carbon nanotubes, excel in power density and longevity but suffer from lower energy density due to non-faradaic charge storage. Pseudocapacitors, by contrast, rely on transition-metal oxides and transition-metal dichalcogenides (TMDs) to achieve higher specific capacitance *via* faradaic reactions. Hybrid supercapacitors that combine EDLC and pseudocapacitive mechanisms have also been developed to bridge the gap between power and energy density, achieving improved performance.[5]

One of the critical factors influencing supercapacitor performance is the choice of electrode material. Among TMDs, molybdenum disulfide (MoS_2) attracted significant interest due to its high surface area, tunable electronic properties, and narrow bandgap (1.2–1.9 eV).[6] This bandgap allows MoS_2 to function as a semiconductor with unique electrochemical properties appropriate for charge storage.[7] While MoS_2 exhibits promising electrochemical properties, its moderate electrical conductivity and limited active-site density limit its practical application in supercapacitors.[7] To address these limitations, doping strategies can be explored. Transition metal doping has proven effective in modifying the electronic structure, enhancing conductivity, and introducing additional active sites. For example, tungsten (W) doping in various materials significantly improves their electrochemical performance. In W-doped $Co(OH)_2$, tungsten facilitated the formation of dandelion-like structures, resulting in specific capacitance values

---

[a] *National Institute for Isotopic and Molecular Technologies, Donat 67-103, Cluj-Napoca, Romania. E-mail: arpad.rostas@itim-cj.ro*
[b] *Doctoral School of Physics, Babes-Bolyai University, Mihai Kogalniceanu 1, Cluj-Napoca, Romania*
[c] *Doctoral School of Chemistry, Babes-Bolyai University, Mihai Kogalniceanu 1, Cluj-Napoca, Romania*
[d] *Faculty of Engineering and Natural Sciences, Sabanci University, Tuzla, Istanbul, Turkey*

of 1051 F g^{-1}, along with excellent cyclic stability and charge retention (92% after 5000 cycles).[8] Similarly, W-doped NiO nanosheets exhibited a high specific capacitance of 872.32 F g^{-1}, with good charge–discharge retention and cyclic stability (87.5% after 3000 cycles).[9] These results underscore the significant impact of W doping on the material's electrochemical properties.

Recent studies on TMD-based hybrid materials have further demonstrated that tungsten doping enhances supercapacitor performance. For instance, a W-doped $MoSe_2$ synthesized *via* the hydrothermal method showed good electrochemical properties with a capacitance of 444.4 mF cm^{-2} at 1 mV s^{-1}.[10] These findings highlight the importance of TMD doping with tungsten to enhance energy storage capabilities. Elemental doping has been shown to improve the electrochemical properties of MoS_2. For example, Gd-doped MoS_2 nanosheets demonstrated a specific capacitance of 357 F g^{-1} at 10 mV s^{-1} and retained 81.5% of their capacity after 5000 cycles.[11] Similarly, Fe-doped MoS_2 exhibited significantly enhanced performance, with 8% Fe-doped samples achieving a specific capacitance of 545 F g^{-1} at 1 A g^{-1} and 84.8% retention over 2000 cycles.[12] Nickel-doped MoS_2, at 10% Ni content, showed a specific capacitance of 156.8 mF cm^{-2} at 4 mA cm^{-2} with a moderate cycling stability of 77.83% after 5000 cycles.[13]

Despite the extensive literature on metal-doped MoS_2, tungsten has not been explored as a substitutional dopant in the MoS_2 lattice for supercapacitor applications. Existing W-containing MoS_2 systems reported in the literature either use WS_2/MoS_2 heterostructures[14] or incorporate W-substituted MoS_2 within polymers such as PEDOT:PSS,[15] all measured under three-electrode conditions in acidic electrolytes. The use of a low W doping concentration (<1%) in 2H-MoS_2 nanoflowers, assembled into a symmetric alkaline supercapacitor device without conductive additives or polymer binders, has not been addressed. Additionally, comprehensive reviews of MoS_2-based supercapacitor electrodes confirm that low electrical conductivity, layer restacking, and limited cycling stability remain the primary unresolved challenges in the field.[7,16] The present work directly addresses this gap by synthesizing MoS_2:W nanoflowers across a doping range of 0–1% *via* a simple one-step hydrothermal route and correlating the W-induced structural modifications characterized by XRD, Raman, EPR, XPS, and BET with electrochemical performance in a symmetric two-electrode configuration using 6 M KOH, without any auxiliary conductive additives.

Thus, this study investigates tungsten-doped molybdenum disulfide (MoS_2:W) as a high-performance electrode material for supercapacitors. Incorporating tungsten is expected to enhance electronic conductivity, increase the density of active sites, and improve structural stability during charge–discharge cycling. A combination of advanced characterization techniques was employed to fully understand these effects. UV-Vis spectroscopy was used to examine the optical properties and potential bandgap shifts,[17] while X-ray diffraction (XRD) provided insight into crystalline phase formation and lattice changes.[18] Raman spectroscopy helps estimate defect sites and structural ordering at the vibrational level.[19] X-ray photoelectron (XPS) and electron paramagnetic resonance (EPR) spectroscopy were applied to study the elemental composition, oxidation states, and the presence of vacancies.[20,21] Finally, comprehensive electrochemical characterization using cyclic voltammetry (CV), electrochemical impedance spectroscopy (EIS), and galvanostatic charge–discharge (GCPL) allowed for the evaluation of charge storage behavior and cycling stability.[22] These complementary methods provide a comprehensive understanding of how tungsten doping modifies the physical and electrochemical properties of MoS_2, thereby enhancing energy-storage performance.

2 Materials and methods

2.1 MoS_2 W-doped materials synthesis

MoS_2 nanoparticles were obtained by the hydrothermal technique as depicted in Scheme 1. To synthesize MoS_2, 3 mmol of ammonium heptamolybdate – $(NH_4)_6Mo_7O_{24}\cdot 4H_2O$ and corresponding molar percentages (0, 0.3, 0.5, 0.7, and 1%) of W powder were stirred continuously for 30 min. Separately, 5 mmol of thiourea ($SC(NH_2)_2$) were dissolved in 20 ml of water. The two solutions were combined, and 20 mL of ethanol was added to the mixture, which was then stirred for 10 min. The resultant mixture was then transferred to a 250 ml autoclave, sealed, and stored in an oven at 180 °C for 18 h. The filling ratio of the autoclave was maintained at 24% for all experiments. Although the pressure inside the autoclave was not directly measured, it is known that, under hydrothermal conditions, pressure is governed by the reaction temperature and the solution volume. By keeping both the temperature and the filling ratio constant across all samples, we ensured consistent pressure conditions across experiments. After gradual cooling, the black powder was centrifuged and cleaned with a water–alcohol solution (1 : 1 v : v). The produced powder was then dried at 65 °C for 12 h. Five samples were synthesized for this study, denoted with MoS_2:Wx, where x = 0, 0.3, 0.5, 0.7, and 1 represent the W doping concentration.

2.2 Morpho-structural characterization methods

A Hitachi HD-2700 microscope was used to examine the morphology of both undoped and W-doped MoS_2 samples *via* scanning transmission electron microscopy (STEM). A BelSorp MaxX equipment (Microtrac BEL Corporation, Japan) was used to record the N_2 sorption isotherms. Pretreatment of samples consisted of degassing under vacuum at 200 °C for 4 h. The standard BET method was employed to calculate the specific surface area (p/p_0 range: 0.02–0.25), and the total pore volume was estimated at p/p_0 = 0.95. The pore size distribution was analyzed with the Barrett–Joyner–Halenda (BJH) method from the desorption branch. X-ray diffraction (XRD) measurements were conducted using a Smart Lab Rigaku diffractometer with Cu-Kα radiation, covering the range 10–90°, with a step size of

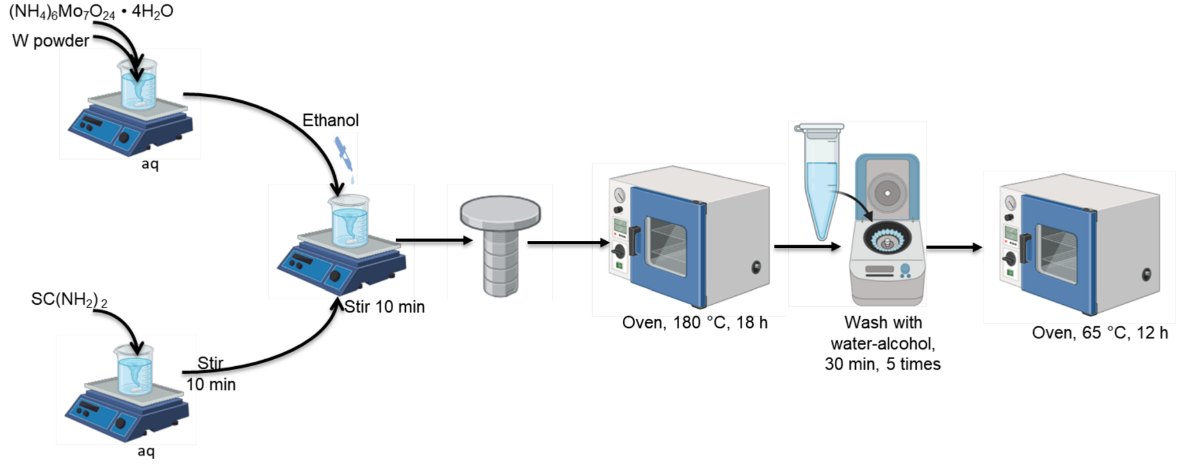

Scheme 1 Schematic illustration of the synthesis procedure employed to synthesize the undoped and W-doped MoS_2 compounds.

0.01°. Raman spectroscopy of both undoped and W-doped MoS_2 samples was performed using a Renishaw InVia Raman system paired with a Leica microscope. The excitation source was a 785 nm near-infrared (NIR) diode laser. The Raman measurements covered a wavenumber range of 100–1100 cm^{-1} with a spectral resolution of 1 cm^{-1}. Experiments used a laser exposure time of 1 s and a single acquisition at 65 mW. Electron paramagnetic resonance (EPR) spectroscopy was carried out at room temperature using a dual-band Bruker E-500 ELEXSYS spectrometer operating at an X-band frequency of 9.88 GHz. Consistency was maintained by ensuring identical conditions and sample quantities across measurements. The qualitative and quantitative composition of the samples was investigated using a custom-built SPECS XPS spectrometer with an Al anode (1486.68 eV) as the X-ray source. Sample preparation was done by ethanol casting onto a sample holder. Spectral analysis was performed using CASA, incorporating relative sensitivities, transmission factors, and electronic mean-free-path factors.

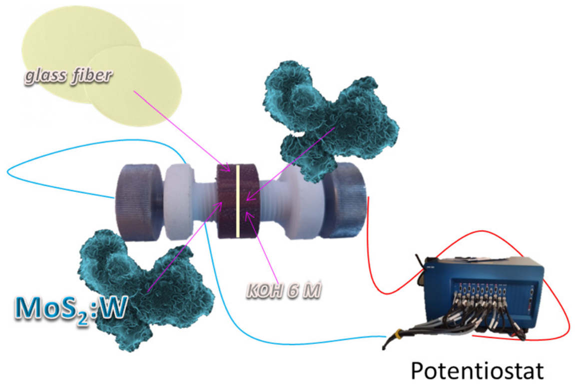

Scheme 2 Schematic representation of the supercapacitor cells employed in this study, highlighting the main components: undoped and W-doped MoS_2 with a 6 M KOH electrolyte and a glass fiber separator between the electrodes.

2.3 Supercapacitive properties characterization methods

Symmetric all-in-one supercapacitor devices were assembled using undoped and W-doped MoS_2 with a 6 M KOH electrolyte and a glass fiber separator between the electrodes as schematically depicted in Scheme 2. Circular stainless-steel bolts on both sides of the device served as current collectors. The areal mass loading of the electrodes on this device is approximately 2.65 mg cm^{-2}, with a total mass of 3 mg per electrode. Electrode thickness was not specifically measured, as the focus was on maintaining a constant mass loading and electrolyte volume (3 mg of active material in 200 μL of 6 M KOH). A BioLogic VMP 300 electrochemical workstation was used to evaluate the electrochemical performance of the electrode materials in a two-electrode system.

The techniques included cyclic voltammetry (CV), potentiostatic electrochemical impedance spectroscopy (PEIS), and galvanostatic cycling with potential limitation (GCPL). CV measurements were performed over a voltage window of 0–1 V, with scan rates ranging from 2 to 200 mV s^{-1}. PEIS measurements were performed with an AC signal amplitude of 10 mV over a frequency range from 10 mHz to 1 MHz. GCPL tests were conducted at a current density of 0.8 A g^{-1}, and the energy and power densities were determined from CV and GCPL data. Because the supercapacitor design was symmetric, specific capacitance, energy, and power density were calculated using the mass of a single electrode to quantify each electrode's contribution. The specific capacitance value can be calculated using the area under the CV curve using the following equation: $C_s = \frac{\int_{V_1}^{V_2} I(V)\mathrm{d}V}{2mK\Delta V}$, where C_s is the specific capacitance, $\int_{V_1}^{V_2} I(V)\mathrm{d}V$ represents the area under the CV curve, m is the mass of the active electrode material, K is the scan rate at which the CV was acquired and ΔV is the voltage window. Using the specific capacitance value, the energy density was calculated with: $E_D = \frac{1}{2}C_s \cdot V^2$, where E_D is the energy density, C_s is the specific capacitance, and V is the potential window, while the power density was calculated with the following equation: $P_D = \frac{E_D}{t}$, where P_D is the power density, and t is the discharge time obtained from the GCPL measurements. This approach ensures that both the electrode series configuration and the electrode mass are properly accounted for, thereby avoiding overestimation of energy and power densities.

3 Results and discussion

The MoS_2 morphology was determined by STEM microscopy. Also, a compositional analysis of the samples was performed with EDS. In Fig. 1(a) and S1, SEM and TEM images with different magnifications, corresponding to the undoped and W-doped MoS_2 samples, are presented, where the formation of layered spherical structures resembling rose flowers is observed, indicating that the dopant dose not alter the morphology in the used concentration range. During the hydrothermal reaction, the MoO_4^- ions and ammonium ions NH_4^+ are released from the precursor ammonium molybdate, and sulfur is derived from thiourea. The MoO_4^- ions react with the S_2^- ions to form MoS_2, while residual ammonia intercalates into the layered structure, thus preventing the stacking of MoS_2 nanostructures and leading to the formation of a spherical structure resembling a rose flower as it was also observed in several previous studies.[23–25] At larger sizes, it is evident that the flowers show flakes/wrinkles on the surface, and the size of the MoS_2:W flowers varies in the range of 270 to 320 nm.

Fig. 1(b) depicts the EDS images showing the distribution of the elements in the MoS_2:W1 sample. The presence of the constituent Mo and S atoms and the uniform distribution of the dopant W ions in the MoS_2 particles can be observed. The same morphological characteristics can be observed in all synthesized MoS_2:W samples, regardless of the W doping degree (data not presented).

The structural properties of the MoS_2 samples were analyzed by X-ray diffraction. The obtained diffractograms are presented in Fig. 1(c). The presence of three broad peaks located at 11, 34, and 58° can be observed, which correspond to reflections on the (002), (103), and (110) planes of MoS_2 according to ICDD: 00-037-1492 supporting the formation of MoS_2 with

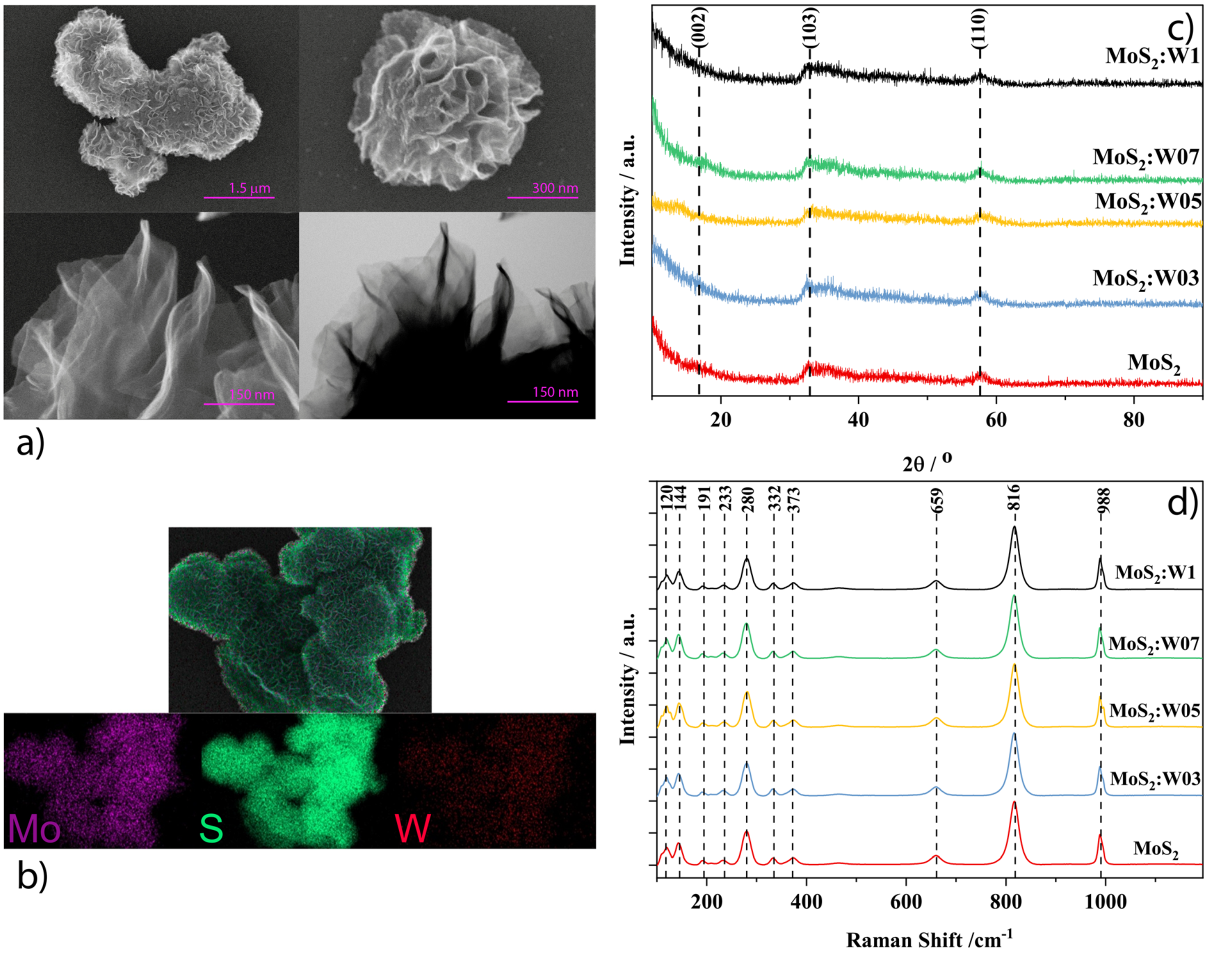

Fig. 1 STEM micrographs at different magnifications (a) and EDS mapping (b) results of the MoS_2:W1 sample. XRD (c) and Raman spectra (d) of the undoped and W-doped MoS_2 samples.

trigonal symmetry belonging to the *P*63/*mmc* space group.[26,27] Molybdenum(IV) sulfide can exist in several polymorphic states: 2H, 1T, and 3R, all possessing a layered structure formed by MoS_6 units.[28] The 2H-MoS_2 polymorphic state, belonging to the space group *P*63/*mmc*, is the most thermodynamically stable phase.[29] To determine the lattice changes, the *d*-spacing value was calculated from the (110) peak of the diffractograms for the analyzed samples. A very slight variation in *d* spacing is observed for doping levels below 0.7%, followed by a more significant increase at 1% W-dopant level as depicted in Table 1.

The Raman spectra of W-doped MoS_2 (Fig. 1(d)) exhibit 10 visible bands at 120 cm^{-1}-[$A_{1g}(\Gamma)$–$E_{1g}(\Gamma)$], 144 cm^{-1}-[E_{1g}(M)–TA (M)], 191 cm^{-1}-ZA(M), 233 cm^{-1}-LA(M), 280 cm^{-1}-$E_{1g}(\Gamma)$, 332 cm^{-1}-E_{2u}(M), 373 cm^{-1}-$E_{2g}{}^{1}(\Gamma)$, 659 cm^{-1}-[$E_{1g}(\Gamma)$ + $E_{2g}{}^{1}(\Gamma)$], 816 cm^{-1}-2 × $A_{1g}(\Gamma)$, 988 cm^{-1}.[30,31] No visible differences are observed; therefore, a Gaussian deconvolution is applied to enhance visualization of the changes. Table 1 presents the deconvolution results for two bands that are more likely to be affected by the dopant: 120 and 373 cm^{-1}. The full width at half maximum (FWHM), peak position, and intensity of these bands were analyzed. In pristine MoS_2, the $A_{1g}(\Gamma)$–$E_{1g}(\Gamma)$ band has a FWHM of 16.09 cm^{-1} and for the $E_{2g}{}^{1}(\Gamma)$ band, it was 19.835 cm^{-1}. After doping, significant changes were observed for these parameters. In particular, the FWHM of the $E_{2g}{}^{1}(\Gamma)$ mode increased significantly in MoS_2:W0.3 (23.19 cm^{-1}) and MoS_2:W0.5 (23.124 cm^{-1}) samples, suggesting increased disorder due to the replacement of Mo by W, which affects the concentration of sulfur vacancies. Sulfur vacancies are known to impact the $E_{2g}{}^{1}(\Gamma)$ mode more prominently due to their effect on the in-plane vibrations of the lattice.[32] However, the FWHM of the $A_{1g}(\Gamma)$–$E_{1g}(\Gamma)$ mode, associated with out-of-plane vibrations,[33] decreased until 0.7% W dopant concentration. This observation implies that W doping introduces an order along the out-of-plane axis.

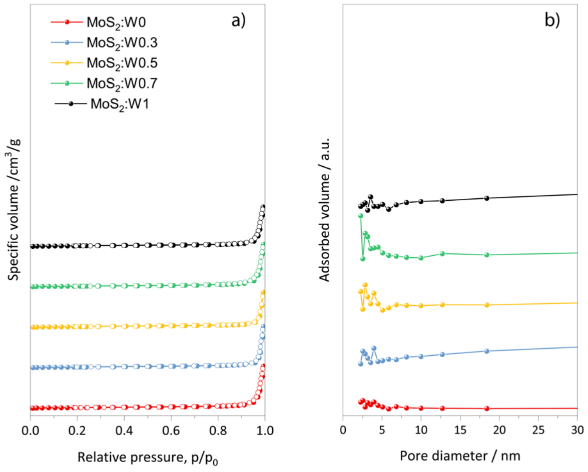

Fig. 2 Nitrogen adsorption–desorption measurements results (a) and pore volume distribution of the undoped and W-doped MoS_2 samples.

The textural characteristics of the undoped and W-doped MoS_2 samples were analyzed using nitrogen adsorption–desorption measurements presented in Fig. 2a. The specific surface area (S_{BET}) and total pore volume (V_p) of the samples are summarized in Table 1 and Fig. 2(b). Pristine MoS_2 shows a specific surface area of 3.52 m^2 g^{-1} and a total pore volume of 0.0075 cm^3 g^{-1}. Upon W doping, the surface area and pore volume vary slightly: S_{BET} ranges from 3.28 to 3.58 m^2 g^{-1}, and V_p ranges from 0.0060 to 0.0076 cm^3 g^{-1}. The MoS_2:W0.7 sample exhibits the highest values, indicating the largest interlayer spacing and highlighting the presence of additional accessible sites for the electrolyte. Beyond this concentration, the surface area and pore volume decrease slightly, as in the case of MoS_2:W1. This effect can be explained by an excessive W content in the lattice, which increases structural disorder and promotes partial restacking or aggregation of the nanoflowers, thereby limiting pore accessibility.

EPR spectroscopy was used to further analyze the presence of defect centers in the materials and the oxidation states of the elements. Fig. 3(a) presents the X-band EPR spectra of pristine and W-doped MoS_2 samples measured at room temperature. The vertical lines indicate two resonances at g = 1.93, characteristic of Mo^{4+} ions and at g = 2.007, representing sulfur defects.[34] The intensity of these EPR signals is constant when the W-doping concentration is varied, and no additional W^{5+} EPR signals are observed, indicating that the dopant ions are EPR silent (W^{4+} with d^2 or W^{6+} with d^0 electron configurations) or not observable due to fast relaxation times. Heavy ions like Tungsten have very strong spin–orbit coupling, which, in high-symmetry sites, often results in closely spaced energy levels, allowing the electron spin to flip too quickly and leading to short relaxation times.[35,36] Thus, the presence of W^{5+} cannot be ruled out at this point.

Table 1 Textural properties of the undoped and W-doped MoS_2 samples, showing the BET specific surface area calculated in the 0.02–0.25 p/p_0 range, and the total pore volume calculated at p/p_0 = 0.95. Results of the Gaussian deconvolution of the Raman spectra of W-doped MoS_2

					$A_{1g}(\Gamma)$–$E_{1g}(\Gamma)$			$E_{2g}{}^{1}(\Gamma)$		
Sample	d/Å	Mo : S	S_{BET}/m^2 g^{-1}	V_p/m^3 g^{-1}	Pos.	Int.	FWHM	Pos.	Int.	FWHM
MoS_2	1.5964	0.507	3.52	0.0075	—	—	—	—	—	—
MoS_2:W0.3	1.5967	0.539	3.28	0.0060	119.763	0.268	16.090	373.300	0.092	19.835
MoS_2:W0.5	1.5963	0.538	3.47	0.0060	119.139	0.287	12.205	372.873	0.106	23.190
MoS_2:W0.7	1.5959	0.533	3.58	0.0076	119.226	0.332	12.176	373.654	0.114	23.124
MoS_2:W1	1.5988	0.539	3.53	0.0068	119.272	0.297	11.846	372.894	0.110	21.170

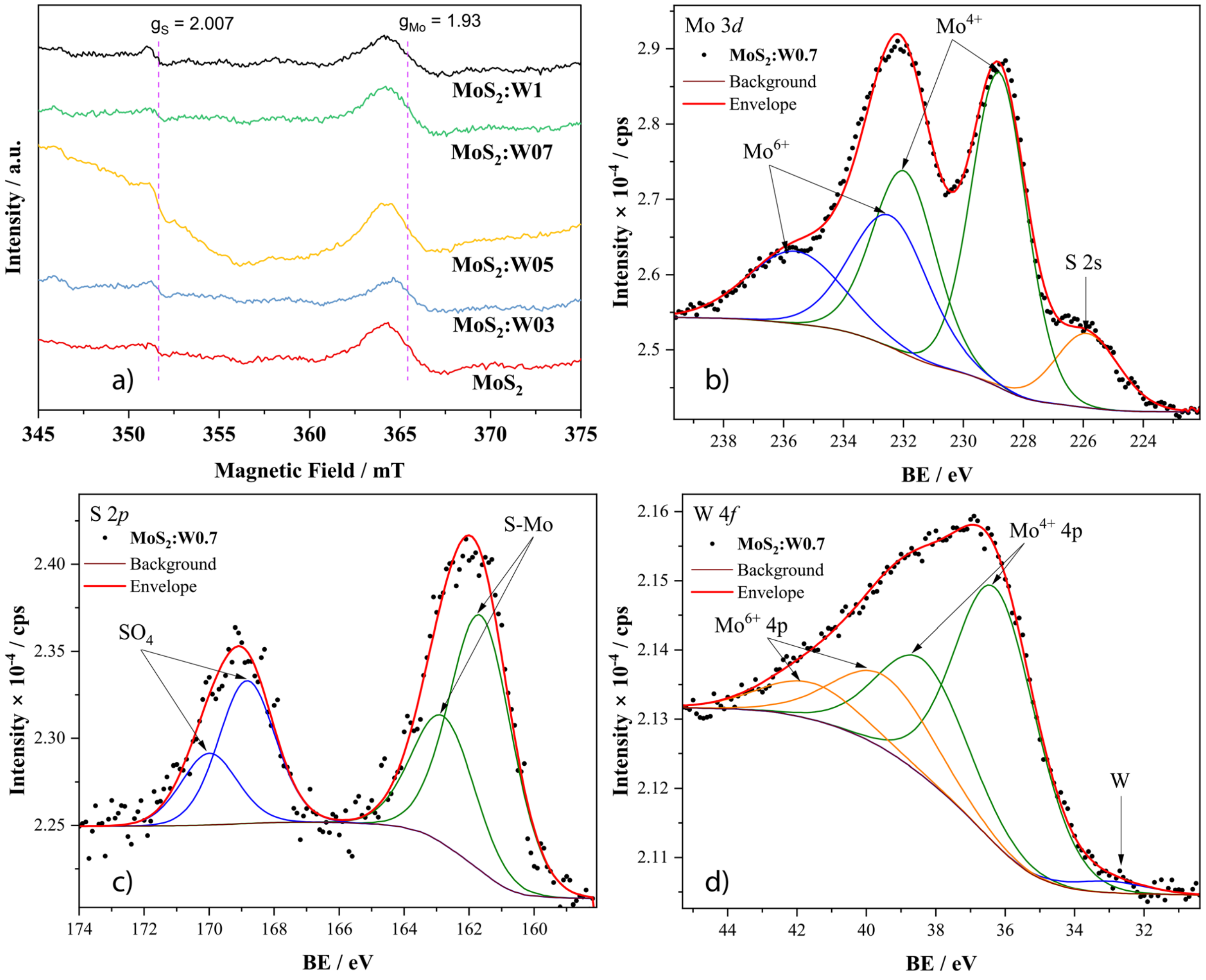

Fig. 3 X-band electron paramagnetic resonance spectra of pristine MoS_2 and W-doped MoS_2 samples recorded at room temperature.

The surface composition for the MoS_2:W0.7 sample was analyzed by XPS. Fig. 3(b) shows the deconvolution of the Mo 3d spectrum. Mo 3d5/2 positioned at 228.8 eV and 3d3/2 positioned at 232.0 eV are characteristic of the Mo^{4+} oxidation state. In comparison, at higher binding energies, another doublet is observed at 232.5 eV (3d5/2) and 235.6 eV (3d3/2), which are characteristic of the Mo^{6+}. Also, at lower binding energies, the S 2s peak is observed at 225.9 eV. The S 2p spectrum deconvolution (Fig. 3(c)) reveals that besides the expected S–Mo lines, an additional SO_4 is also present in the sample, which comes from the synthesis reagents. Fig. 3(d) shows the W 4f spectrum. In this case, the Mo 4p signal strongly overlaps with the W 4f signal, complicating deconvolution. Mo^{4+} is positioned at 36.3 eV (4p3/2) and 38.4 eV (4p1/2), while Mo^{6+} is positioned at 39.5 eV (4p3/2) and 41.6 eV (4p1/2). The W 4f line positioned at 33.0 eV has a broad HWHM of 2.5 eV, indicating that multiple oxidation states could be present: mostly W^{4+}, W^{5+}, and probably W^{6+} as compared to existing literature.[37–39] The calculated atomic ratio W/Mo^{4+} is 0.0035, which is in good agreement with the nominal concentration of 0.7% W, given that XPS detects the surface of the materials and not the bulk. The sulfur vacancy concentration was estimated from the Mo : S ratio (see Table 1). At W doping levels below 1%, the Mo : S ratio remains near the stoichiometric value of the pristine sample, though it indicates a slight sulfur deficiency, in good agreement with the EPR results, where the EPR signal intensities remain constant with varying W-dopant concentration.

The electrochemical behavior of pristine and W-doped MoS_2 samples was investigated using cyclic voltammetry (CV), galvanostatic charge–discharge (GCPL), electrochemical impedance spectroscopy (EIS), and the Dunn method to evaluate charge storage mechanisms. All measurements were performed on a symmetric supercapacitor device with a two-electrode configuration, using a 6 M KOH electrolyte and glass fiber as the separator. The mass of the electrode material is 3 mg over an area of 1.13 cm^2.

Fig. 4(a)–(e) shows the CV curves measured at different scan rates for the undoped and W-doped MoS_2-based SC devices across the voltage window of 0–1 V. The CV curves for all SC devices exhibit non-ideal quasi-rectangular shapes as exemplified in Fig. 4(f) at a scan rate of 100 mV s^{-1}, indicative of a

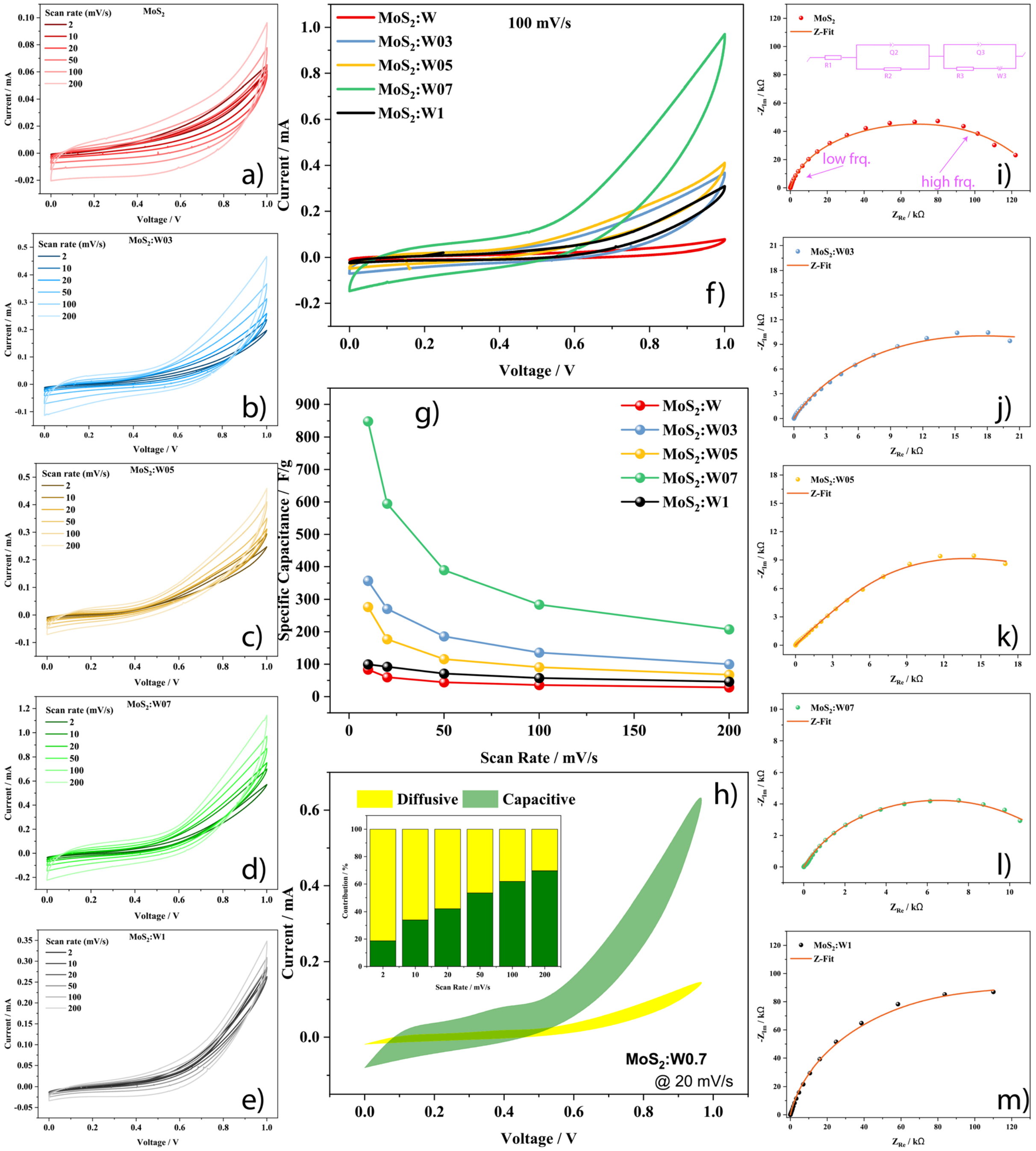

Fig. 4 CV results measured at scan rates varying from 2 to 200 mV s^{-1} (a)–(e) and compared at 100 mV s^{-1} (f), specific capacitance as a function of the CV scan rate (g) for the undoped and W-doped MoS_2-base symmetric SC devices. Dunn's analysis results of the MoS_2:0.7-based symmetric SC device, with the inset showing the diffusive and capacitive contributions at different scan rates (h). Nquist plots together with the Z-fit results of the undoped and W-doped MoS_2 based SC devices (i)–(m) measured with an AC signal amplitude of 10 mV over a frequency range from 10 mHz to 1 MHz.

combined electric double-layer and pseudocapacitive behavior.[40] As reported in the literature, ideal supercapacitor behavior exhibits a rectangular shape associated with the EDLC charge-storage phenomenon.[41] The CV curve changes as the W-dopant concentration increases; the undoped MoS_2-based SC device exhibits a CV curve closest to EDLC-type behavior; however, W doping induces a significant shift in the CV curve, indicating an increased contribution of pseudocapacitance. W doping introduces defects, edge sites, and additional redox centers as described above, contributing to this deviation from the non-ideal shape. A high degree of retention of the curve shape at elevated scan rates, particularly for the MoS_2:W0.7-

based SC device, indicates good rate capability, arising from efficient charge transfer and rapid ion transport. Furthermore, the nearly symmetric anodic and cathodic profiles across the scan-rate range also indicate high electrochemical reversibility. The deviation from an ideal rectangular profile reflects the influence of faradaic surface redox reactions, which are particularly enhanced by W doping, as evidenced by the redox peaks that primarily occur at the electrode surface. Secondly, internal resistance among the device's components causes edge rounding, a common observation in practical supercapacitors.[42]

The trend of the CV curves suggests the positive influence of W doping on MoS_2, as we observed the increased current response with increasing doping concentration (see Fig. 4(f)), with the highest current response obtained for the MoS_2:W0.7-based SC device, and further increase of the doping concentration tends to decrease the current values. The MoS_2:W0.7-based SC device also exhibits the largest CV area, which is directly related to its specific capacitance. The performance trend indicates that W doping improves electrical conductivity and produces more accessible active sites up to an optimal concentration for redox reaction to take place, after which excess dopant can cause agglomeration or structural distortion, which negatively affects the charge transport.[43]

Fig. 4(g) presents the specific capacitance (C_s) as a function of the scan rate, calculated from the CV curves as presented in section 2.3. The MoS_2:W0.7-based SC device exhibited the highest capacitance at all scan rates, reaching a maximum of 848 F g^{-1} at 10 mV s^{-1}. The undoped MoS_2-based device exhibits the lowest specific capacitance.

To gain a deeper understanding of the operating mechanism of the best-performing MoS_2:W07-based SC device, Dunn analysis was applied,[44] and the results are presented in Fig. 4(h). The equation used to express the different contributions to the measured current is expressed as $I(V) = k_1 \cdot \nu + k_2 \cdot \sqrt{\nu}$, where $k_1 \cdot \nu$ represents the capacitive current, $k_2 \cdot \sqrt{\nu}$ shows the diffusive current, and ν represents the scan rate. The relative contributions of each mechanism can be determined by examining the slope and intercept of a Dunn plot, corresponding to the constants k_1 and k_2.[45]

The inset of Fig. 4(h) shows that the diffusion-controlled mechanism dominates at all scan rates, contributing approximately 59% at 200 mV s^{-1}. The diffusive and capacitive contributions calculated from the Dunn analysis for all other devices are presented in Fig. S2. Contributions from both mechanisms are visible across all devices, with a slightly higher capacitive contribution at high scan rates in the W-doped MoS_2-based SC devices. For all devices, the diffusion contribution increased at lower scan rates, indicating that ions had sufficient time to diffuse in the material. This trend suggests that diffusion-limited pseudocapacitive processes primarily govern charge storage, rather than surface-controlled reactions. The persistence of a strong diffusion-controlled response at high scan rates implies that the W-doped MoS_2 structure facilitates rapid ion intercalation and access to internal redox-active sites, likely due to expanded interlayer spacing and defect-assisted transport pathways.[46] These characteristics reflect the favorable structural and electronic modifications introduced by W doping, as observed in other studies, in which W ions enhanced the charge-storage properties of $Co(OH)_2$ by introducing redox-active sites. Hence, as a result, the specific capacitance is increased twice that of pristine $Co(OH)_2$.[8]

Electrochemical impedance spectroscopy (EIS) probes the charge-transfer and ion-diffusion behavior of the MoS_2:W-based SC devices. Nyquist plots of the tested devices are shown in Fig. 4(i)–(m), showing that all devices form an incomplete semicircle, contrary to the ideal EDLC-type behavior, which shows a near-vertical Nyquist plot in the low-frequency region. Similar to CV, this deviation can be explained by the internal resistance of components in real devices and by pseudocapacitance.[47] The diameter of the semicircle is associated with the charge-transfer resistance, R_{ct}, and we observed that the undoped MoS_2 and MoS_2:W1-based SC devices exhibit the largest diameter. In contrast, the other devices show a low-diameter semicircle. Consistent with the CV observation, the best-performing MoS_2:W0.7-based SC device exhibits the smallest semicircle, indicating the lowest charge-transfer impedance. The x-intercept in the high-frequency region corresponds to the solution resistance R_s. Here, the MoS_2:W0.7-based SC device exhibits the lowest R_s, whereas the undoped MoS_2-based SC device exhibits the highest R_s. Moderate W doping significantly reduced both R_s and R_{ct}, with MoS_2:W0.3, W0.5, and W0.7 showing the lowest impedance values. This suggests enhanced electron/ion transport kinetics and reduced internal resistance, thereby improving electrochemical performance.[11] The Nyquist plots of all devices do not exhibit a well-defined Warburg region in the mid-frequency range, typically associated with ion-diffusion limitation.[48] This can probably be due to the layered morphology of MoS_2, which provides short ion diffusion pathways as

Table 2 Equivalent circuit values obtained from Z-fitting of the Nyquist plots, and energy (E_D) and power (P_D) density values of the undoped and W-doped MoS_2

Sample	R_1/Ω	$C_{dl}/\mu F$	R_2/Ω	$W_2/\Omega\ s^{-0.5}$	$C_{sp}/F\ g^{-1}$	E_D/Wh kg^{-1}	P_D/W kg^{-1}
				@10 mV s^{-1}			
MoS_2	2.45	12.03	1495	544	83.34	11.57	208.36
MoS_2:W 0.3%	0.346	84.78	284	192	357.03	49.58	892.58
MoS_2:W 0.5%	0.313	15.95	14.14	143	276.68	38.42	691.71
MoS_2:W 0.7%	0.252	448	190	98	848.53	117.85	2121
MoS_2:W1%	0.461	52.53	1668	789	99.73	13.85	249

suggested in a previous study,[49] and to the presence of W-induced defects that facilitate faster ion transport as shown by Muthukumar *et al.*,[50] where doping-induced defects lead to faster diffusion of ions. Additionally, in a symmetric two-electrode configuration, the impedance contributions from both electrodes may mask or compress the Warburg region. To further analyze the Nyquist plots and obtain values for the physical parameters, equivalent-circuit fitting was performed; the fitted graphs are shown in Fig. 4(i)–(m), and the equivalent circuit used is shown in the inset of Fig. 4(i). Here, R_1 represents the solution resistance (R_s), R_2 is the charge transfer resistance (R_{ct}), and Q denotes a constant phase element (CPE), which is a more generalized impedance element that accounts for non-idealities in the capacitor's behavior. Q_2 in the circuit is analogous to C_{dl}, which is the double-layer capacitance, while Q_3 represents a pseudo-capacitance. W_3 shows the Warburg impedance from ion diffusion in the electrolyte at the low-frequency region. Table 2 shows the values of the most important parameters for ease of comparison. The MoS_2:W0.7-based SC device exhibited low R_s and R_{ct} values, along with a high C_{dl}, which together contribute to its superior performance relative to the other SC devices evaluated in this study. The devices that showed the lowest performance, MoS_2 and the MoS_2:W1-based SC devices, exhibited higher resistance and Warburg impedance.

GCPL measurements can provide vital information on the discharge time, specific capacity, cyclic stability, and rate capability of the studied SC devices by varying the current density. Fig. 5(a) shows the charge–discharge measurements for all the devices measured at a current density of 0.8 A g^{-1}. Charge–discharge curves also indicate that charge storage in these devices results from a combination of EDLC and pseudocapacitive behavior. The EDLC-type charge–discharge curves normally have a triangle shape,[51] suggesting symmetry in the charge and discharge cycles. However, non-linear features in the charge discharge curves suggest a dominant pseudocapacitive contribution as it was reported in the literature,[51,52] consistent with faradaic redox processes at the Mo and W active sites, especially visible in the best-performing MoS_2:W0.7-based SC device, which not only shows the longest discharge time but also shows a plateau region on maximum voltage in the charge curve, which is associated with the redox activity. The undoped MoS_2-based device shows the shortest discharge time, while all other devices have discharge times that are more or less similar, but far shorter than that of the best-performing device, confirming its superior energy storage capability, in agreement with the CV and EIS results.

Fig. 5(b) shows the cyclic stability where capacitance retention is plotted as a function of the cycle number. All W-doped MoS_2-based SC devices exhibit good capacitance retention, with the lowest retention observed in the MoS_2:W0.5 device, which retains almost 80% after 2000 cycles. All other W-doped SC devices retained more than 90% of their initial capacitance, highlighting tungsten's role in stabilizing the electrode structure. MoS_2:W0.7 again showed the best cycling durability, making it a good candidate for long-term applications. While the undoped MoS_2-based SC device exhibits the lowest retention of about 60% after 2000 cycles, indicating that W doping improves the cyclic stability of MoS_2 when used as an electrode

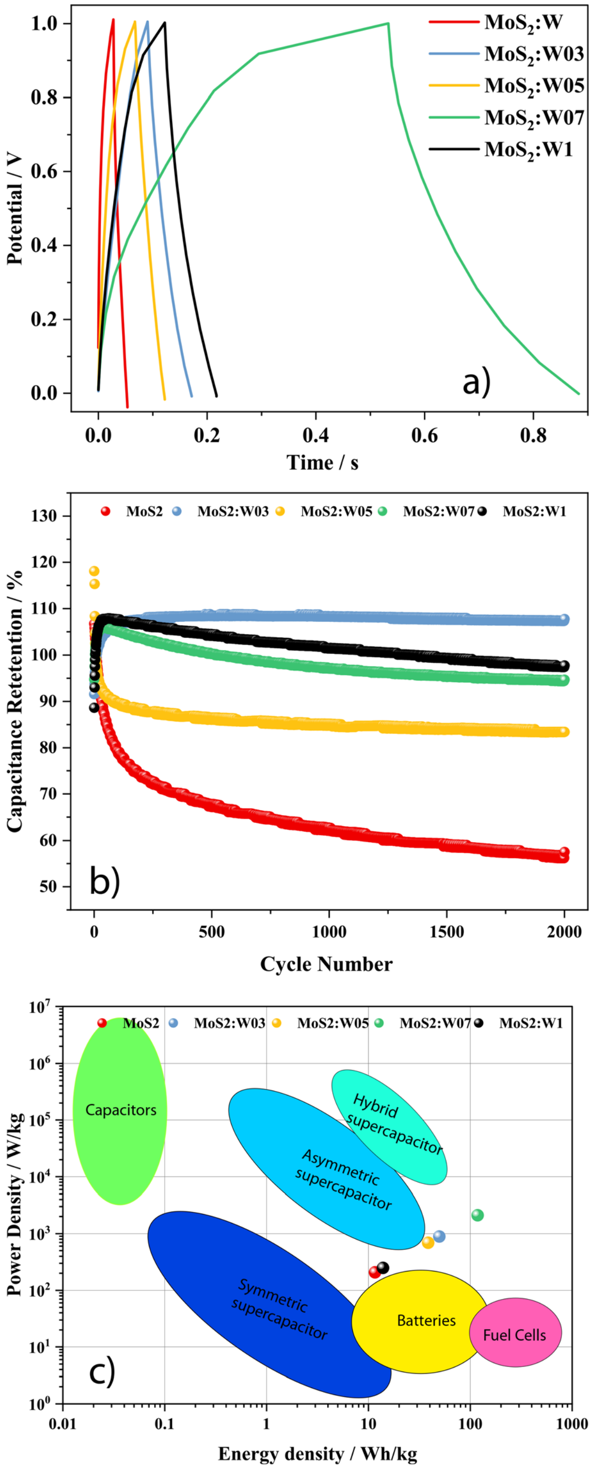

Fig. 5 Charge–discharge curves measured at 0.8 A g^{-1} in the voltage window of 0–1 V for all MoS_2:W samples used as electrode materials for supercapacitors (a), capacitance retention as a function of the cycle number (b), and standard Ragone plot including the performance obtained in this study (c).

material in symmetric SC devices. Cyclic performance measured over 10 000 cycles at 3 A g^{-1} is presented in Fig. S3 to further test the devices' cyclic performance. The trend remains similar to that observed for 2000 cycles, in which the W-doped MoS_2-based SC devices showed better retention than the undoped MoS_2-based SC devices. The lowest retention for the MoS_2-based SC device was almost 75% after 10 000 cycles.

The improved cycling stability of W-doped MoS_2 can be attributed to several synergistic structural effects. W incorporation induces lattice distortion and defect formation, disrupting the strong van der Waals interactions between MoS_2 layers and thereby preventing restacking during repeated charge–discharge cycles, helping to maintain a high electrochemically active surface area over prolonged cycling. Substituting Mo with W enhances the lattice's structural integrity, as W incorporation stabilizes the MoS_2 framework against mechanical degradation during repeated ion insertion and extraction. Additionally, W doping alters the local electronic structure, potentially suppressing the dissolution or surface degradation of Mo species in the alkaline electrolyte. These combined effects ensure stable ion transport pathways and sustained accessibility of redox-active sites, resulting in the observed high capacitance retention over extended cycling.

The Ragone plot is a standard metric for comparing energy storage devices, plotting the power density of the SC devices as a function of their energy density. Table 2 presents the energy and power density values for all devices, and Fig. 5(c) plots these values in a standard Ragone plot to better visualize their position in a universal comparison. As expected, the MoS_2:W0.7-based SC device exhibits the highest energy and power densities, whereas the undoped MoS_2 devices show the lowest performance. The best-performing MoS_2:W0.7 in the Ragone plot shows energy density values approaching the fuel cell zone, suggesting significant potential for this electrode material.

Compared with other doped MoS_2-based electrodes listed in Table 3, the MoS_2:W0.7 sample, developed in this study, exhibits superior electrochemical performance, delivering a specific capacitance of 848 F g^{-1} at 10 mV s^{-1} and an energy density of 117.85 Wh kg^{-1}. These values exceed those reported for most dopants such as Gd, Fe, Ni, and Co, and are comparable to oxide-based composites like MoS_2:MnO_2 and MoS_2:SnO_2. This confirms the positive role of W incorporation, making the material a promising candidate for high-performance energy storage applications.

The structural and morphological characteristics of the W-doped MoS_2 samples can be directly correlated with their electrochemical behavior. SEM and TEM images (Fig. 1(a)) reveal a flower-like structure composed of thin, curved MoS_2 sheets. This 3D nanoflower morphology provides numerous exposed edges and open spaces, facilitating easier interaction with electrolyte ions. BET measurements support this observation, showing that the surface area increases with W doping up to 0.7%, indicating enhanced ion transport accessibility. Defect centers are also known to improve the electrochemical properties of materials.[60–62] Raman and EPR spectroscopy evidence the presence of sulfur-defect centers induced by the dopant. The presence of multivalent Mo and W dopant ions was evidenced by XPS measurements, in which molybdenum appears in two oxidation states, +4 and +6, and tungsten appears in two oxidation states, +5 and +6. All these structural modifications are reflected in the CV curves, where the highest current responses are observed for the 0.5 and 0.7% W-doped samples. The presence of W in different oxidation states facilitates faradaic reactions within the electrode material, as evidenced by higher specific capacitance values for the two devices. Dunn's analysis of the best-performing MoS_2:W0.7-based device reveals a prominent contribution from diffusive and capacitive mechanisms, further supporting our CV results. The Nyquist plots show that the MoS_2:W0.7 sample exhibits the lowest imaginary impedance, as well as the lowest R_s and R_{ct}, suggesting faster ion diffusion and more active sites, related to the sulfur vacancies and the presence of the multivalent Mo and W elements. Charge–discharge data reveal the longest discharge time and high cyclability for the best-performing MoS_2:W0.7-based SC device.

Table 3 C_{sp}, E_D, P_D, and cycling stability of supercapacitor devices using doped MoS_2 electrode materials reported in the recent literature, compared with the present work

Material	C_{sp}/F g^{-1}	E_D/Wh kg^{-1}	P_D/W kg^{-1}	Cycling stability	Config.	Ref.
MoS_2:Gd	357@10 mV s^{-1}	—	—	81.5%/5000 cycles	3E	11
MoS_2:Fe	545@1 A g^{-1}	—	—	84.8%/2000 cycles	3E	12
MoS_2:Ni	425@5 mV s^{-1}	9	0.5	—	3E	53
MoS_2:Co	164@1 A gv	3.67	3279.97	—	2E-S	54
MoS_2:Sr	489.75@1 A g^{-1}	31	5760	62.5%/2000 cycles	2E-A	55
MoS_2:Cu	402.7@1 A g^{-1}	94.5	2880	88.77%/10 000 cycles	2E-A	56
MoS_2@FeS_2	386@1 A g^{-1}	53	699	90.3%/10 000 cycles	2E-S	57
MoS_2:MnO_2	515@1 A g^{-1}	15	10 000	—	—	58
MoS_2:SnO_2	826.5@1 mV s^{-1}	14.4	4000	—	—	59
W-MoS_2/PEDOT:PSS	845.14@1 A g^{-1}	—	—	89%/10 000 cycles	3E	15
MoS_2:W	848@10 mV s^{-1}	117.85	2121	97%/2000 cycles	2E-S	t.w.

Abbreviations: 3E – three-electrode half-cell; 2E-S – two-electrode symmetric device; 2E-A – two-electrode asymmetric device; t.w. – this work.

4 Conclusions

This work presents the influence of tungsten doping on the structure, defect concentration, and defect types, and how these changes relate to the electrochemical performance of MoS_2 nanoflowers used in symmetric supercapacitors. Morpho-structural characterization, like XRD, STEM, and XPS, shows a successful incorporation of W ions in the MoS_2 lattice. Raman and EPR spectroscopy analyses of the synthesized materials demonstrated that W incorporation into the MoS_2 lattice alters the defect environment, particularly sulfur defects, and shifts the oxidation state of Mo with increasing W concentration. BET measurements reveal changes in specific surface area and pore size with increasing W doping concentration. Finally, to evaluate the electrochemical performance of the synthesized samples, all-in-one symmetric supercapacitor devices were assembled and characterized using CV, GCPL, and EIS. The results show an increase in performance with increased W doping, with the maximum performance obtained for the 0.7% W-doped-based SC device, showing specific capacitance of 848 F g^{-1} at 10 mV s^{-1}, with excellent stability of 97% capacitance retention after 2000 cycles and good balance of energy density (117.8 Wh kg^{-1}) and power density (2121 W kg^{-1}). All these results confirm the potential of these materials for next-generation energy storage devices. Overall, this study demonstrates that controlling the tungsten doping concentration is an effective approach for tuning the structural and, consequently, the electrochemical properties of MoS_2. Thus, defect and dopant engineering in transition-metal dichalcogenide materials is a good strategy for high-performance supercapacitor applications.

Author contributions

I Nesterovschi: formal analysis, investigation, writing – original draft, writing – review & editing, visualization; AU Ammar: formal analysis, investigation, data curation, writing – original draft, writing – review & editing; A Popa: formal analysis, investigation, writing – original draft, writing – review & editing; M Stefan: formal analysis, investigation; D Toloman: formal analysis, investigation, writing – original draft, writing – review & editing; SG Macavei: formal analysis, investigation; Cristina Leostean: formal analysis, investigation, writing – original draft, writing – review & editing; L Barbu Tudoran: formal analysis, investigation; M Mihet: formal analysis, investigation; A Varadi: formal analysis, investigation; E Erdem: formal analysis, investigation, validation, supervision; AM Rostas: conceptualization, validation, formal analysis, investigation, data curation, writing – original draft, writing – review & editing, visualization, supervision.

Conflicts of interest

The authors declare that they have no known competing financial interests or personal relationships that could have appeared to influence the work reported in this paper.

Data availability

The data supporting this article have been included in the manuscript.

Supplementary information (SI) is available. See DOI: https://doi.org/10.1039/d6nr00405a.

Acknowledgements

The authors would like to express appreciation for the financial support of the Ministry of Research, Innovation and Digitalization, Romania's National Recovery and Resilience Plan, PNRR-III-C9-2022-I8, CF 163/15.11.22, financing contract no. 760097/23.05.23.

References

1 M. A. Dar, S. Majid, M. Satgunam, C. Siva, S. Ansari, P. Arularasan and S. R. Ahamed, *Int. J. Hydrogen Energy*, 2024, **70**, 10–28.
2 J. Zhang, M. Gu and X. Chen, *Micro Nano Eng.*, 2023, **21**, 100229.
3 H. R. Khan and A. L. Ahmad, *J. Ind. Eng. Chem.*, 2025, **141**, 46–66.
4 D. Meena, R. Kumar, S. Gupta, O. Khan, D. Gupta and M. Singh, *J. Energy Storage*, 2023, **72**, 109323.
5 S. Mandal, A. B. Mendhe, H. M. Rakhade, N. S. Barse, M. Roy, P. Rosaiah, T. Park, H.-S. Lee, A. C. Mendhe and D. Kim, *Chem. Eng. J. Adv.*, 2025, **21**, 100690.
6 K. B. M. Ismail, M. Arun Kumar, S. Mahalingam, J. Kim and R. Atchudan, *Materials*, 2023, **16**, 4471.
7 I. T. Bello, D. Tsotetsi, B. Shaku, O. Adedokun, D. Chen and M. S. Dhlamini, *J. Energy Storage*, 2024, **103**, 114355.
8 G. Nabi, *et al.*, *Mater. Sci. Eng., B*, 2024, **299**, 117015.
9 R. Ahmed, G. Nabi, N. Khalid, F. Ali and M. Tanveer, *Appl. Nanosci.*, 2021, **11**, 1279–1289.
10 Q. Liu, J. Ning, H. Guo, M. Xia, B. Wang, X. Feng, D. Wang, J. Zhang and Y. Hao, *Nanomaterials*, 2021, **11**, 1477.
11 M. Isacfranklin, L. E. M. Princy, Y. Rathinam, L. Kungumadevi, G. Ravi, A. G. Al-Sehemi and D. Velauthapillai, *Energy Fuels*, 2022, **36**, 6476–6482.
12 M. R. Charapale, U. V. Shembade, S. A. Ahir, V. P. Kothavale, N. T. Jadhav, V. G. Sankpal, P. P. Waifalkar, A. V. Moholkar, T. D. Dongale and S. A. Masti, *Surf. Interfaces*, 2024, **52**, 104814.
13 A. Panghal, D. Sahoo, D. Deepak, S. Deshmukh, B. Kaviraj and S. S. Roy, *ACS Appl. Nano Mater.*, 2024, **7**, 5358–5371.
14 Ö. Yağci, M. B. Arvas and S. Yazar, *Mater. Chem. Phys.*, 2025, **332**, 130223.
15 C. Gunasekaran, G. Shanmugam and S. Sreedhar, *J. Mater. Chem. A*, 2026, **14**, 12713–12727.
16 M. B. Askari and P. Salarizadeh, *Materials for Renewable and Sustainable Energy*, 2025, **14**, 55.

17 M. Farooq and T. Iqbal, *J. Inorg. Organomet. Polym. Mater.*, 2022, **32**, 4422–4433.

18 R. Rahman, D. Samanta, A. Pathak and T. K. Nath, *RSC Adv.*, 2021, **11**, 1303–1319.

19 J. Zou, Z. Cai, Y. Lai, J. Tan, R. Zhang, S. Feng, G. Wang, J. Lin, B. Liu and H.-M. Cheng, *ACS Nano*, 2021, **15**, 7340–7347.

20 J. Aliaga, P. Vera, J. Araya, L. Ballesteros, J. Urzúa, M. Farías, F. Paraguay-Delgado, G. Alonso-Núñez, G. González and E. Benavente, *Molecules*, 2019, **24**, 4631.

21 M. K. Singh, P. Chettri, A. Tripathi, A. Tiwari, B. Mukherjee and R. Mandal, *Phys. Chem. Chem. Phys.*, 2018, **20**, 15817–15823.

22 I. T. Bello, K. O. Otun, G. Nyongombe, O. Adedokun, G. L. Kabongo and M. S. Dhlamini, *Nanomaterials*, 2022, **12**, 490.

23 F. Wang, M. Zheng, B. Zhang, C. Zhu, Q. Li, L. Ma and W. Shen, *Sci. Rep.*, 2016, **6**, 31092.

24 L. Zhao, Y. Wang, G. Wen, X. Zhang and X. Huang, *J. Colloid Interface Sci.*, 2025, **680**, 151–161.

25 S. Rai, P. Phogat, R. Jha, S. Singh, *et al.*, *Mater. Chem. Phys.*, 2025, **329**, 130147.

26 S. Sharifi, K. Rahimi and A. Yazdani, *Sci. Rep.*, 2021, **11**, 8378.

27 B. Qu, Y. Sun, L. Liu, C. Li, C. Yu, X. Zhang and Y. Chen, *Sci. Rep.*, 2017, **7**, 42772.

28 C. D. Quilty, L. M. Housel, D. C. Bock, M. R. Dunkin, L. Wang, D. M. Lutz, A. Abraham, A. M. Bruck, E. S. Takeuchi, K. J. Takeuchi, *et al.*, *ACS Appl. Energy Mater.*, 2019, **2**, 7635–7646.

29 T. Stephenson, Z. Li, B. Olsen and D. Mitlin, *Energy Environ. Sci.*, 2014, **7**, 209–231.

30 H. Li, Q. Zhang, C. C. R. Yap, B. K. Tay, T. H. T. Edwin, A. Olivier and D. Baillargeat, *Adv. Funct. Mater.*, 2012, **22**, 1385–1390.

31 M. Placidi, M. Dimitrievska, V. Izquierdo-Roca, X. Fontané, A. Castellanos-Gomez, A. Pérez-Tomás, N. Mestres, M. Espindola-Rodriguez, S. López-Marino, M. Neuschitzer, *et al.*, *2D Mater.*, 2015, **2**, 035006.

32 W. M. Parkin, A. Balan, L. Liang, P. M. Das, M. Lamparski, C. H. Naylor, J. A. Rodríguez-Manzo, A. C. Johnson, V. Meunier and M. Drndic, *ACS Nano*, 2016, **10**, 4134–4142.

33 A. P. Nayak, T. Pandey, D. Voiry, J. Liu, S. T. Moran, A. Sharma, C. Tan, C.-H. Chen, L.-J. Li, M. Chhowalla, *et al.*, *Nano Lett.*, 2015, **15**, 346–353.

34 J. R. Gonzalez, R. Alcantara, J. L. Tirado, A. J. Fielding and R. A. Dryfe, *Chem. Mater.*, 2017, **29**, 5886–5895.

35 F. E. Mabbs and D. Collison, *Electron paramagnetic resonance of d transition metal compounds*, Elsevier, 2013, vol. 16.

36 A. Abragam and B. Bleaney, *Electron paramagnetic resonance of transition ions*, OUP oxford, 2012.

37 K. Ahmad, W. Raza, M. Q. Khan and R. A. Khan, *React. Kinet., Mech. Catal.*, 2024, **137**, 2363–2374.

38 A. Hasani, Q. V. Le, T. P. Nguyen, K. S. Choi, W. Sohn, J.-K. Kim, H. W. Jang and S. Y. Kim, *Sci. Rep.*, 2017, **7**, 13258.

39 X.-Y. Chen, Y. Zhao, Z.-H. Liu, Y.-T. Pang, D.-G. Wei, J.-Y. Wangchen and C.-B. Yao, *Appl. Surf. Sci.*, 2025, **682**, 161686.

40 A. Noori, M. F. El-Kady, M. S. Rahmanifar, R. B. Kaner and M. F. Mousavi, *Chem. Soc. Rev.*, 2019, **48**, 1272–1341.

41 J. P. A. dos Santos, F. C. Rufino, J. I. Y. Ota, R. C. Fernandes, R. Vicentini, C. J. Pagan, L. M. Da Silva and H. Zanin, *J. Energy Chem.*, 2023, **80**, 265–283.

42 H. Wang and L. Pilon, *Electrochim. Acta*, 2012, **64**, 130–139.

43 K. S. Bhat, P. Mukesh, A. P. Hegde, A. Kumar, K. Brijesh, H. Nagaraja, *et al.*, *Ionics*, 2025, **31**, 4955–4969.

44 R. Raavi, S. Archana, P. A. Reddy and P. Elumalai, *Energy Adv.*, 2023, **2**, 385–397.

45 W. Pholauyphon, P. Charoen-Amornkitt, T. Suzuki and S. Tsushima, *Electrochem. Commun.*, 2024, **159**, 107654.

46 S. Fan, Y. Gong, S. Chen and Y. Zhang, *Micromachines*, 2025, **16**, 754.

47 A. Allison and H. Andreas, *J. Power Sources*, 2019, **426**, 93–96.

48 A. C. Lazanas and M. I. Prodromidis, *ACS Meas. Sci. Au*, 2023, **3**, 162–193.

49 H. Ganesha, S. Veeresh, Y. Nagaraju, M. Vandana, M. Basappa, H. Vijeth and H. Devendrappa, *Nanoscale Adv.*, 2022, **4**, 521–531.

50 K. Muthukumar, L. Leban, A. Sekar, A. Elangovan, N. Sarkar and J. Li, *Sustainable Energy Fuels*, 2021, **5**, 4002–4014.

51 O. Gerard, A. Numan, S. Krishnan, M. Khalid, R. Subramaniam and R. Kasi, *J. Energy Storage*, 2022, **50**, 104283.

52 V. Augustyn, P. Simon and B. Dunn, *Energy Environ. Sci.*, 2014, **7**, 1597–1614.

53 S. J. Panchu, K. Raju, P. Singh, D. D. Johnson and H. C. Swart, *ACS Appl. Energy Mater.*, 2023, **6**, 2187–2198.

54 I. T. Bello, K. O. Otun, G. Nyongombe, O. Adedokun, G. L. Kabongo and M. S. Dhlamini, *Int. J. Energy Res.*, 2022, **46**, 8908–8918.

55 E. Tom, A. Velluva, A. Joseph, T. Thomas, M. S. Sha, P. Jithin, D. Thomas, K. K. Sadasivuni and J. Kurian, *J. Electron. Mater.*, 2025, **54**, 451–461.

56 K. Prakash, S. Kamalakannan, J. Archana, M. Navaneethan and S. Harish, *J. Energy Storage*, 2024, **102**, 114173.

57 A. Singh, M. Iqbal, K. S. Hazra and S. K. Mahapatra, *Energy Fuels*, 2024, **38**, 4666–4675.

58 M. M. H. Raza, A. S. Alzahrani, M. Al-Rasheidi, M. Y. Bhat and F. Khan, *J. Alloys Compd.*, 2025, 182265.

59 M. M. H. Raza, A. S. Alzahrani, M. Al-Rasheidi, S. Nayer and F. Khan, *Electrochim. Acta*, 2025, 147264.

60 A. U. Ammar, M. Stefan, S. G. Macavei, S. Tripon, O. Pana, C. Leostean, I. D. Vlaicu, A. M. Rostas and E. Erdem, *J. Mater. Sci.: Mater. Electron.*, 2023, **34**, 98.

61 A. U. Ammar, A. Popa, D. Toloman, S. Macavei, A. Ciorita, A.-E. Bocirnea, M. Stan, E. Erdem and A. M. Rostas, *ACS Appl. Eng. Mater.*, 2024, **2**, 126–135.

62 D. Toloman, A. Gungor, A. Popa, M. Stefan, S. Macavei, L. Barbu-Tudoran, A. Varadi, I. D. Yildirim, R. Suciu, I. Nesterovschi, *et al.*, *Ceram. Int.*, 2025, **51**, 353–365.